Laboratory–Numerical Model Comparisons of Flow over a Coastal Canyon

NICOLAS PÉRENNE

Environmental Fluid Dynamics Program, Department of Mechanical and Aerospace Engineering, Arizona State University, Tempe, Arizona

DALE B. HAIDVOGEL

Institute of Marine and Coastal Sciences, Rutgers, The State University of New Jersey, New Brunswick, New Jersey

DON L. BOYER

Environmental Fluid Dynamics Program, Department of Mechanical and Aerospace Engineering, Arizona State University, Tempe, Arizona

(Manuscript received 10 December 1999, in final form 5 January 2000)

ABSTRACT

Different modeling approaches are applied to the same geophysical flow in order to assess the ability of laboratory models to provide useful benchmarks in the development of oceanic numerical models. The test case considered here—that of the flow driven by an oscillatory forcing over a submarine canyon—involves background rotation, density stratification, and steep topography. Velocity fields measured by particle-tracking velocimetry and time series of density fluctuations are directly compared to the corresponding outputs from a high-order finite-element numerical ocean model.

Quantitative comparison of the laboratory and numerical models shows good overall agreement in the structure and magnitude of the strongest residual currents, which occur at the level of the shelf break in the configuration presented here. The associated residual vorticity field is also structurally consistent between the two models, although the residual divergence is not. Residual currents higher up and lower down in the water column are weaker than at the shelf break, and the agreement between the laboratory and numerical models is less good at these levels, possibly indicative of the controlling influence of the surface and bottom boundary layers.

1. Introduction

It is now commonplace in fluid dynamics research to test numerical model results against associated laboratory experiments. In this way it has been possible to develop sophisticated aerospace vehicles that perform very closely to the predictions of numerical models. For example, Reed et al. (1998) review the numerous studies addressing the transition to turbulence over airfoils in which the results from direct numerical simulations are quantitatively compared to experimental data.

While aerodynamic flows are quite complex, they in general do not contain the wealth of physical processes at work in a geophysical environment. One reason for the greater complexity of geophysical flows (compared with, say, aerodynamic studies of airfoils) is the larger number of dimensionless parameters associated with those systems: geophysical flows involve (i) highly complex terrain having a wide range of characteristic length scales, (ii) background rotation and stratification, (iii) forcings that are nonuniform in both space and time, and (iv) complex turbulence characteristics of the background motions. In such a context, improved numerical models are essential to achieve better predictive capabilities for such problems as the dispersion of passive scalars and pollutants in atmospheric or oceanic flows, and issues related to the processes affecting climate change.

Perhaps the single investigation that was most influential in motivating the present study was that of Haidvogel and Beckman (1998) in which the results of different numerical coastal models were compared for the same system geometry and background flow conditions. The geometry chosen was a channel model with a continuous shelf, shelf break, and continental slope incised by a single submarine canyon. The flow was driven by an oscillatory alongshelf wind stress, and both homo-

Corresponding author address: Dr. Don Boyer, Department of Mechanical and Aerospace Engineering, College of Engineering and Applied Sciences, Arizona State University, Tempe, AZ 85287-6106. E-mail: don.boyer@asu.edu

geneous and linearly stratified flow situations were considered. The models were compared by determining the mean flow generated by each of them. The intermodel comparisons were satisfactory in a qualitative sense for the homogeneous (constant density) case, although quantitative differences in magnitude of the residual velocity vectors were large. (The various numerical estimations for the alongshore residual transport differed by a factor of 6.) For the stratified case, the models were not even in qualitative agreement. In order to determine when the model is ''right'' then, one must seek datasets to be used in the numerical model development and as tests for these models.

The most satisfying approach would be to use the field data available on submarine canyons, the most recent and comprehensive survey being by Hickey (1997). It is fair to say, however, that the field data currently available cannot provide the detailed information in space and time that is necessary to implement well-conditioned, quantitative tests for numerical models. This lack of field data with sufficient spatial and temporal resolution for quantitative numerical model testing is also a problem in other atmospheric and oceanic contexts. As an alternative, numerical analysts have relied on testing their models against analytical and other numerical models. The use of analytical models for such purposes, however, is quite limited owing to the fact that flows with the requisite physics of rotation, stratification, steep and complex topography, and unsteady background forcing are often analytically intractable.

The thesis of the present line of inquiry is that laboratory models have the potential for providing the critical datasets needed by numerical analysts in the development of environmental models generally, and, in the present context, coastal circulation models in particular. Adequate realization of this goal requires that the laboratory model must (i) have both background rotation, stratification, and steep topography; (ii) provide synoptic data with sufficient spatial and temporal resolution; and (iii) be carefully analyzed with regard to the repeatability and inherent error of the laboratory experiments. Clearly if laboratory data are to serve as benchmarks in numerical model development, the experiments must be repeatable to an adequate level of accuracy.

Earlier reports have provided ample motivation for the study of the interaction of coastal flows with submarine canyons; see for instance Hickey (1995, 1997), Boyer et al. (1999), and most recently She and Klinck (2000), and Klinck and She (1999, manuscript submitted to *J. Geophys. Res.*). The latter article, in particular, is a numerical study of the instantaneous flow fields that are driven in a submarine canyon by a time-varying wind forcing, a situation that is close to the one considered here. The interested reader is referred to these articles for background information on the investigation of flows in the vicinity of coastal canyons.

This paper is organized as follows: section 2 lists the parameters that are common to both numerical and laboratory models; sections 3 and 4, respectively, give some technical information about the laboratory and numerical models; section 5 then describes the laboratory data, which are compared to the numerical results in section 6; and some concluding remarks are made in section 7.

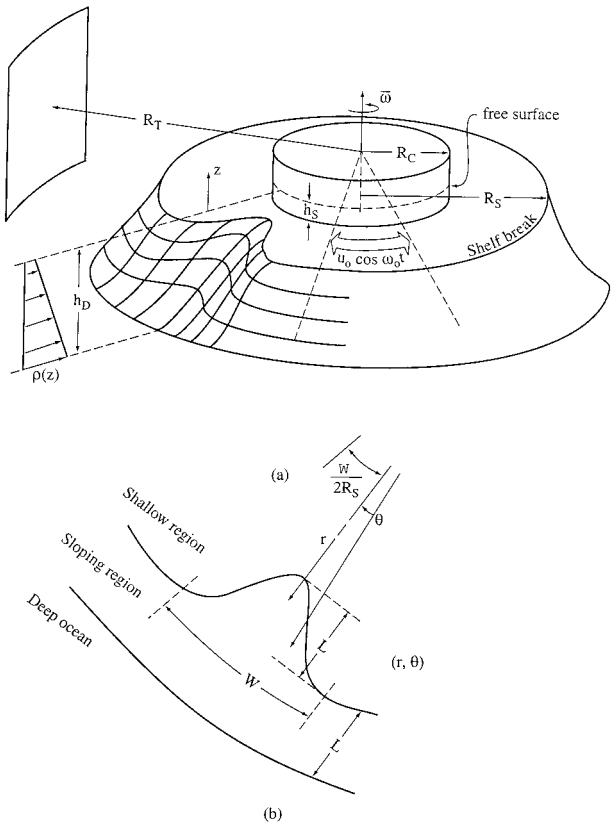

FIG. 1. Numerical and physical models: (a) schematic diagram and (b) top view.

2. External parameters and similarity considerations

a. Physical system and external parameters of the problem

The numerical model was configured to match, as closely as possible, all aspects of the laboratory experiments: the physical system [Fig. 1; see also Boyer et al. (1999) for a detailed description] is the same for both models and consists of a circular continental shelf/slope geometry, interrupted by a single canyon; the equations were solved at the laboratory scale and the laboratory forcing was implemented in the numerical model (section 4). In order to focus on the concept of laboratory–numerical model comparisons, only one set of parameters is considered in this article. The consequences of varying these parameters will be the subject of a subsequent paper.

TABLE 1. Dimensional values for the laboratory–numerical model and its oceanic ''prototype.'' The first and second values of viscosities mentioned in the second column are for the laboratory and numerical models, respectively. The numerical model also includes a bottom stress parameterization (see text). The oceanic values of the forcing parameters T and U stand for a prototype situation of wind forcing (tidal currents have their main component at superinertial frequencies and can be stronger).

Parameter	Models	Oceanic prototype
R_C (radius of the coast)	35 cm	—
R_S (radius at the shelf break)	55 cm	—
R_T (radius of the test tank)	90 cm	—
h_s (depth over the shelf)	2.5 cm	150 m
h_D (maximum depth)	12.5 cm	600 m
W (width of the canyon	20 cm	7 km
L (length of the canyon)	15 cm	15 km
f (Coriolis parameter)	0.25 s^{-1}	10^{-4} s^{-1}
N (typical Brunt–Väisälä frequency)	2.5 s^{-1}	5 10^{-3} s^{-1}
ν_H (horizontal viscosity)	0.01 cm^2 s^{-1}, 1 cm^2 s^{-1}	0.01 cm^2 s^{-1}
ν_V (vertical viscosity)	0.01 cm^2 s^{-1}, 0.01 cm^2 s^{-1}	80 cm^2 s^{-1}
T (timescale of the forcing)	24 s	From a day to several months
U (alongshore velocity forced at the shelf break)	1 cm s^{-1}	10–30 cm s^{-1}

1) GEOMETRIC PARAMETERS

The topography is defined analytically using ''$\cos^2$'' functions [Boyer et al. 1999, Eq. (2.2)]. This introduces (i) two vertical length scales—h_s and h_D, which are the minimum and maximum depths of the model, respectively; and (ii) two horizontal length scales—W and L, which are the ''width'' and ''length'' of the canyon, respectively (Fig. 1b). The values of these-dimensional parameters are listed in Table 1. From these, one can define three nondimensional geometric ratios to characterize the topographic scales: (h_s/h_D), the fractional depth; (h_D/W), the vertical aspect ratio; and (W/L), the horizontal aspect ratio. The values of these nondimensional numbers are listed in Table 2.

One could also introduce the radius at the shelf break, R_s (see Fig. 1), as another characteristic length scale in our models. This brings in the parameter (W/R_s), which defines the curvature of the model geometry. This parameter is studied extensively in Boyer et al. (1999) and it is concluded that the leading-order flow (in a Rossby number development) is not affected by the curvature terms.

2) BACKGROUND PARAMETERS

The mean rotation rate of the turntable was not varied during the experiments; the model is rotating counterclockwise (seen from above), leading to a positive (Northern Hemisphere) value of the Coriolis parameter: $f = 0.50$ s^{-1}. The typical Brunt–Väisälä frequency of the experiments is $N = 2.5$ s^{-1}. The resulting Burger number,

$$\mathrm{Bu} = \frac{N^2 h_D^2}{f^2 W^2},$$

has a value close to 10 (Table 2).

The importance of viscous effects can be characterized by an Ekman number defined as

$$\mathrm{Ek} = \frac{\nu}{f h_S^2},$$

which is based on the depth above the continental shelf and either the horizontal or vertical viscosity. The viscosity that applies in the physical model is of course the same in all directions (i.e., the laminar viscosity of water; cf. Table 1). In contrast, the finite spatial resolution of the numerical model requires enhancement of the viscosity above molecular levels. In principle, the numerical model seeks to represent all important scales present in the laboratory flow, with the possible exception of the bottom frictional boundary layer. This goal would seem to be achievable here because the flow appeared to be quite laminar in the laboratory experiments, which did not exhibit significant turbulence at scales so

TABLE 2. Nondimensional parameters for the laboratory/numerical model and its oceanic prototype.

Parameter	Models	Oceanic prototype
h_s/h_D (fractional depth)	0.20	0.25
h_D/W (vertical aspect ratio)	0.63	0.086
W/L (horizontal aspect ratio)	1.33	0.47
$\mathrm{Bu} = N^2h_D^2/(f^2W^2)$ (Burger number)	9.8	18
$E_H = \nu_H/(fh_s^2)$	3.2×10^{-3}, 0.32	4×10^{-7}
$E_V = \nu_V/(fh_s^2)$	3.2×10^{-3}, 3.2×10^{-3}	4×10^{-3}
$\mathrm{Ro}_t = (2\pi/T)/f$ (temporal Rossby number)	0.52	<1
$\mathrm{Ro} = U/(fW)$ (Rossby number)	0.10	0.14–0.43

small that they would obviously be missed by the numerical model. In the vertical direction, we used a combination of (i) laminar viscosity ($\nu = 0.01$ cm^2 s^{-1}) and (ii) a bottom stress parameterization to represent the (laminar) bottom boundary layer that occurs in the laboratory flow. The parameterization used is a linear function of the horizontal velocity:

$$\tau = -\rho_0\left(\sqrt{\frac{\nu f}{2}}\right)^{1/2} u_h = -(0.05)u_h.$$

This is inspired by a scaling of the stress that would occur in a sheared flow where the typical velocity is u_h and the typical length scale is $D_E = [(2\nu)/f]^{1/2}$, the height of the Ekman boundary layer. (Here, $D_E = 2$ mm in the physical flow.) Due to computational stability constraints, however, it was not possible to set the horizontal numerical viscosity to the laminar viscosity of water; it was enhanced by a factor of 100 (Table 1).

3) FORCING PARAMETERS

The laboratory forcing is realized by modulating the rotation rate of the turntable. This is equivalent to a body force, described in Boyer et al. (1999), which was introduced into the numerical model. This body force has no vertical or azimuthal dependence, but is proportional to the distance r from the center of the turntable (cf. the appendix). It is shown that, in the absence of the canyon and neglecting viscosity effects, this forcing will lead to a purely azimuthal oscillatory flow, when observed in a reference frame that is fixed to the topography. Two parameters then define the forcing used in the models: (i) the period T of the modulation, and (ii) the amplitude U of the velocity, which is forced at the shelf-break radius, far from the canyon.

The experiments presented here were performed using $T = 24$ s and $U = 1$ cm s^{-1}. One can then define a temporal Rossby number,

$$\mathrm{Ro}_t = \frac{2\pi}{Tf},$$

which is the ratio of the forcing frequency to the Coriolis parameter, and a Rossby number,

$$\mathrm{Ro} = \frac{U}{fW}.$$

The values of Ro_t and Ro are specified in Table 2. With these values, the typical particle excursion is $E = UT/(2\pi) = 3.8$ cm. A Reynolds number based on the forcing velocity U and the excursion E is $\mathrm{Re} = UE/\nu = 380$. This is too small to ensure a transition to turbulence over a flat plate, in accordance with the apparently laminar behavior of the fluid in the laboratory experiments.

b. Oceanic similitude

The determination of the conditions required for our laboratory and numerical experiments to simulate the oceanic situation is quite complex. The question of similitude is important, however, and is now discussed because (i) it helps to place the results in an observational and theoretical perspective, and (ii) the geophysical relevance of the models is an important motivation of this study (laboratory–numerical model comparisons are more common for industrial applications). In order to discuss the oceanic significance of the experiments, we will first define a *simplified* prototype.

1) THE OCEANIC PROTOTYPE

We keep only four parameters to define the bathymetry of the oceanic prototype (previously introduced to describe the model topography). The values chosen (Table 1) are representative of several canyons that have been the focus of oceanographic surveys (Freeland and Denman 1982; Noble and Butman 1989; Hickey 1997).

We consider the prototype canyon to be rotating on an f plane at midlatitude ($f = 10^{-4}$ s^{-1}). The vertical density profile is linear throughout the water column, thereby omitting the effect of, say, the seasonal thermocline. A representative Brunt–Väisälä frequency for our 600-m-deep prototype ocean (Table 1) is $N = 5 \times 10^{-3}$ s^{-1}. The situation being modeled is also simplified in that it includes no background turbulence that would lead to a significant horizontal turbulent diffusion. (Recall that the horizontal scale of our prototype is of the order of a few kilometers.) Small-scale turbulence can arise for many reasons, however (e.g., tidal stirring over rough topography), but this turbulent diffusion is assumed to act mainly in the vertical direction; it is not represented in the models (even in the laboratory one), because (i) the oceanic Reynolds number is much greater than that in the model, and (ii) the oceanic bottom has some roughness whereas the model topography is smooth. Using for instance the parameterization quoted by Davies (1987), a prototype vertical (tidally induced) diffusivity of $\nu_V \sim 80$ cm^2 s^{-1} arises for moderate tidal currents of amplitude 20 cm s^{-1}.

We now discuss the forcing parameters T and U chosen for our canyon prototype. Oceanic observations of flow above submarine canyons, for example, Freeland and Denman (1982), Noble and Butman (1989), and Hickey (1997), are mainly interpreted with reference to wind forcing, the influence of which can be either local or remote owing to the propagation of coastal trapped waves. The time evolution of these forcings can be seasonal (Freeland and Denman, 1982), limited to a few days (upwelling or downwelling ''events''; Hickey 1997), or a combination of various periodic components that can be used to describe a stochastic random forcing at the weather timescale (Noble and Butman, 1989), hence the broad range of timescales mentioned in Table

1. The situation considered here, however, is that of a periodic forcing with a zero mean, involving only one frequency. This is closest to the last of the three situations mentioned above and is also relevant to the forcing exerted by oceanic tides, which includes both sub- and superinertial frequencies. [Concerning tidal currents in submarine canyons, see, for instance, Hunkins (1988).] The focus on oscillatory currents brings in the issue of flow rectification (i.e., the appearance of a residual current due to nonlinearities), which is interesting for at least two reasons: (i) a previous laboratory–numerical study (Pérenne et al. 1997) showed that a rather dramatic rectification could take place in a homogeneous fluid, and it is interesting to see if this rectification is as efficient in the presence of density stratification; and (ii) nonlinear rectification is very challenging for numerical modelers (Haidvogel and Beckman 1998).

Finally, the simplified situation we address is that of a forcing that has very small horizontal and vertical dependence compared to the canyon length scales. The currents are mainly oscillating in the alongshore direction far from the canyon. This can be loosely related to the forcing exerted by the pressure field associated with a barotropic first-mode, coastal-trapped wave. Such a wave could be generated in the ocean by tidal or wind forcing. In the latter case, a more realistic prototype would include stronger spatial variations of the forcing (propagation of baroclinic coastal trapped waves or local forcing by the wind stress applied at the upper surface of the ocean), but would be more difficult to emulate in the laboratory. The amplitude of the currents impinging on our prototype of submarine canyons is in the range of 10–30 cm s^{-1} (Table 1).

2) SIMILITUDE OF THE MODEL WITH THE SIMPLIFIED PROTOTYPE

The fractional depth (h_S/h_D) is well reproduced by the models (Table 2), although there is of course some degree of arbitrariness in the specification of h_D for the oceanic prototype. In contrast, the models have a much greater vertical aspect ratio (h_D/W) than the prototype, because the amplification of the vertical scale is necessary for several reasons when performing laboratory experiments. Provided that the flow is hydrostatic, however, the ratio (h_D/W) disappears from the nondimensional equations of motion and thus is no longer a similarity requirement. A set of conditions for the flow to be hydrostatic was derived by Boyer et al. (1999) in the same experimental context as for the present study and is

$$\left(\frac{h_D}{W}\right)^2 \frac{\mathrm{Ro}^2}{\mathrm{Bu}} \ll 1, \qquad \left(\frac{h_D}{W}\right)^2 \frac{\mathrm{RoRo_t}}{\mathrm{Bu}} \ll 1. \tag{1}$$

From Table 2, these nondimensional quantities equal 4.1 $\times$ 10^{-4} and 2.1 $\times$ 10^{-3}, respectively, which, at least from the point of view of the external flow parameters, indicates that the laboratory experiment is approximately hydrostatic. Hence, oceanic similitude can be realized approximately in spite of the fact that the vertical aspect ratio of the model is elevated.

The horizontal aspect ratio (W/L) is significantly greater in our models than in the prototype (Table 2), meaning that the model canyon is wider than the ''typical'' oceanic canyon defined in section 2b(1). This might have some important dynamical consequences. A canyon with a smaller relative width will be considered in the future.

The Burger number of the prototype canyon is close to 20 (Table 2); this is mainly a consequence of the fact that the topographic scale W is much smaller than the internal radius of deformation. This important specification of the canyon flow problem seems to be quite realistic. [See, for instance, the values mentioned in Hickey (1997).] The model is in reasonable Burger similitude with the ocean since its Burger number is also much greater than 1.

The horizontal Ekman numbers for the oceanic prototype and the laboratory models are both very small although the laboratory flow is more viscous (Table 2). The vertical Ekman numbers have the same order of magnitude (both quite small), if one assumes a reasonable amount of tidally induced turbulence in the prototype, as explained in section 2b(1). The smallness of these Ekman numbers allows one to argue that the flow is not driven by frictional/diffusion effects ''at first order''; however, the residual currents (a ''higher order'' flow feature), might depend on these parameters, even if small. In the numerical model, the horizontal Ekman number is larger than those of both the laboratory model and the oceanic prototype. In the vertical direction, the Ekman number is the same as in the laboratory but recall that the numerical model also includes a bottom stress parameterization. This parameterization, however, should introduce dissipation effects of the same order of magnitude as those corresponding to a real Ekman–Stokes layer, as argued in section 2a(2).

The temporal Rossby number is subinertial (Table 2), in accordance with the timescales induced by, say, wind fluctuations. In the future, we plan to consider higher and lower forcing frequencies. The Rossby number is somewhat low; nonetheless, we will see that the flow is substantially nonlinear.

The similitude of our models with the simplified prototype implies the following rules for conversion of laboratory–numerical dimensional results into oceanic quantities: a model horizontal (vertical) distance of x centimeters corresponds to a prototype distance of $(0.35)x$ kilometers [$(4.8)x$ meters], a duration of 1 s in the model corresponds to 1.4 h in the prototype, a model horizontal or vertical velocity of x centimeters per second corresponds to a prototype velocity of $(7)x$ centimeters per second, and finally a vorticity or divergence of x per second in the model corresponds to a value of $(2 \times 10^{-4})x$ s^{-1} in the prototype.

3. Measurement techniques

The following is a description of the laboratory techniques employed during this study, and of the type of data we have produced using these techniques. Since the issue of accuracy is central to the comparison of numerical and laboratory results, it is worth reviewing the experimental procedure in detail.

a. Time series of density fluctuations

In order to monitor the density field (the establishment of which, using saltwater, will be described in section 3c), an array of density probes was set up in the canyon, and time series of density fluctuations were recorded at various (fixed) locations. These probes (Head 1983) actually measure the conductivity of the water, which is related to its salinity and thus to its density. They are manufactured by Precision Measurement Engineering. The output from the probes is amplified using electronics built at Arizona State University and digitized on a PC computer featuring a digital acquisition system board. This output was directly calibrated against density using solutions of various salinities, the densities of which were known by hydrometer measurement; the densities used in these experiments typically ranges from $\rho \sim 1$ g cm^{-3} (nearly freshwater) to $\rho \sim 1.1$ g cm^{-3} (corresponding to a salinity of $S \sim 130‰$). Over such a range, the calibration curves (voltage output as a function of density) depart slightly from a straight line, but this departure was taken into account.

The locations of the probes are indicated in Fig. 2, which also defines the coordinate system used for the presentation of the velocity field data. The Cartesian coordinate system used here is such that the y axis is along the canyon axis, with $y = 0$ standing where the shelf break would be located if there were no canyon. The x axis is tangent to the circle of radius $r = 55$ cm (the radius of the shelf break) and $x = 0$ is located on the canyon axis. The y coordinate increases in the offshore direction and the x coordinate increases in the direction that will be later referred to as the downstream direction, the direction that leaves the shallow water on its right.

The (horizontal) array of four conductivity probes was placed at various depths inside the canyon. The rack used for this purpose has a spacing of $\Delta x = \Delta y = 2.5$ cm. Probes 2 and 4 are on the canyon axis while probes 1–3 are on the x axis (Fig. 2a). Vertical exploration of the density field was achieved by repeating the same experiment several times and varying the depth of the probes. Three depths will be considered in this article: $z = z_1 = -h_S/2$ is the upper level, located at middepth on the model continental shelf; $z = z_2 = -h_S$ is the level of the shelf break; finally, $z = z_3 = h_S - (h_D - h_S)/4$ is the lower level, located below the canyon rim but still relatively high in the water column (Fig. 2b).

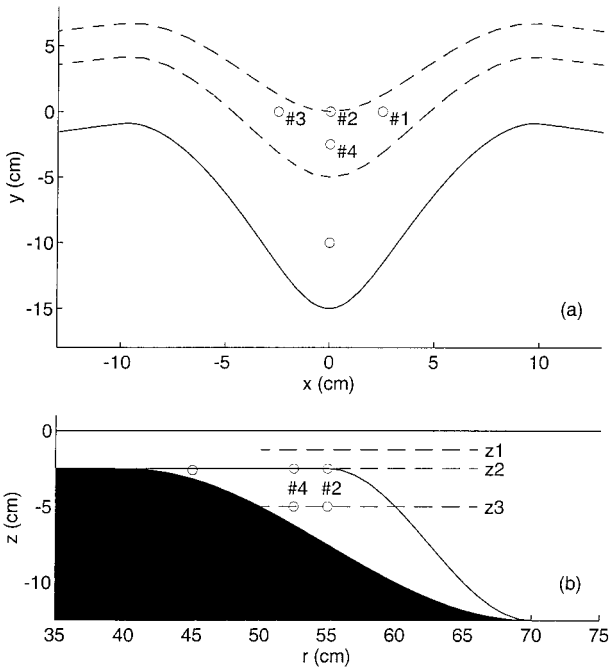

FIG. 2. Schematic diagram of locations of conductivity probes and horizontal velocity measurements: (a) plan view, where the shelf break (solid line) and the $z = -5$ cm and $z = -7.5$ cm isobaths (dashed lines) are shown, and (b) vertical cross section—the topograhic profile of the canyon is shown by the black shaded region, while the continental slope is shown by the curved solid boundary. The horizontal and vertical locations that were systematically explored are numbered 1 to 4, and z_1 to z_3, respectively. A time series of density fluctuations was also recorded at the location defined by the number-free open circle.

The time at which the forcing is initiated was recorded along with the signals from the four probes, thanks to a timing signal derived from the PC controlling the rotation rate of the turntable. The phase of the density fluctuations, relative to that of the forcing, is thus known accurately. The length of the records was typically 900 s in the experiments reported here; the sampling rate was 10 Hz but, in order to remove acquisition noise, the signal was then filtered using a time-averaging window of width equal to 1 s.

The conductivity probes were also used to measure the density profiles just before the experiments (i.e., while the rotation rate of the table is still constant). This background state will be discussed in section 3c, where we will see that for various reasons the density stratification is not linear from top to bottom. However, one can use the background density gradient measured prior to the experiment at the vertical location where the time series will be recorded to convert the density fluctuations into a measure of the vertical displacement of isopycnals:

$$\Delta\eta(t) = \frac{\rho(t) - \overline{\rho}}{-\dfrac{d\overline{\rho}}{dz}}, \tag{2}$$

where $\overline{\rho}(z)$ is the background density profile. This quantity is useful in physical interpretations and/or attempts of comparisons with oceanic observations.

b. Particle-tracking velocimetry

A horizontal light sheet was projected in the fluid at the various levels defined in the previous section, using a standard light source. This light sheet is a few millimeters thick. The fluid was seeded with neutrally buoyant particles and their motion was filmed from above and recorded on an S-VHS video tape recorder. The video tapes were then processed using the Digimage software (Dalziel 1992), which allows for (i) identification of the particles present in the field of view; (ii) tracking[1] of these particle using a sophisticated, cost-minimizing algorithm; and (iii) interpolation/averaging of the randomly spaced Lagrangian measurements onto a regular (Eulerian) grid.

Among all the parameters one has to specify in order to operate Digimage, it is important to mention a few matters regarding step iii. The grid spacing chosen for the interpolation was $\Delta x = \Delta y = 1$ cm. Digimage was also configured so that the (randomly spaced) Lagrangian measurements contributing to the estimation of the Eulerian velocity at a given grid point are those that are located within a circle of radius 2 cm centered on that grid point. (A weight function linearly decaying from 1 to 0 over 2 cm is used, so that the more distant measurements have a lesser contribution.) Thus although many scales might be present in the physical flow, the particle-tracking velocimetry (PTV), as implemented here, samples only the length scales larger than ~1 cm.

A calibration of the Digimage settings was performed using a plate on which some of the particles used in our experiments were glued, the concentration of these particles being close to the one we were able to achieve in the actual experiments. The plate was then rotated with a known vorticity (again, typical of the vorticities observed in the actual experiments) and the velocity and vorticity were recomputed using the PTV. In this situation, the error was found to be ~5% on velocity and ~15% for vorticity.

The tracking was performed on polystyrene particles of density 1.04 ± 0.005 g cm^{-3}. The fact that all these particles do not have exactly the same density was especially useful. Since they float at various levels in the continuous density stratification, there were always particles in the light sheet in spite of the vertical excursions experienced by the fluid during the experiments. To explore the fluid at the various levels, the mean density of the fluid was adjusted so that the particles would float around the level of interest (the vertical density gradient being kept constant). The disadvantage of these particles, however, is their rather large size (diameter ~ 1 mm), which limited to approximately 1000 the number of particles present in the field of view (30×25 cm^2); this limitation is due to the fact that the coalescing tendency of the particles is too strong[2] to allow for higher concentrations. Finally, we note that the measurements at the $z = z_1$ level proved to be difficult because a significant fraction of the particles would then float to the surface.

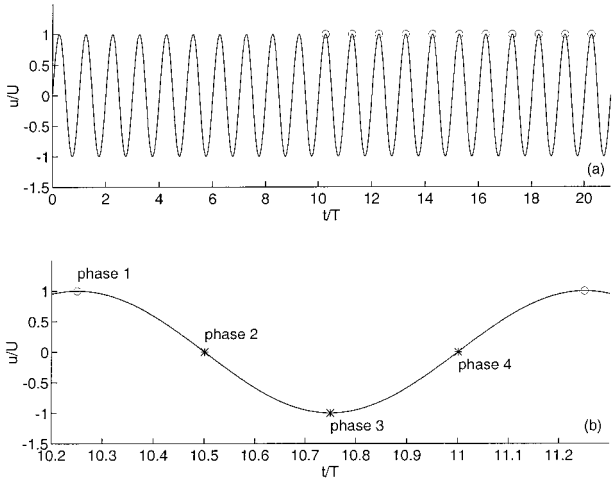

FIG. 3. Temporal averaging of the PTV data: (a) the forcing sequence used in the experiments—the velocity that would be forced at the shelf break in the absence of canyon is plotted, the measurements involves cycles 11–20, phase averaging is thus done over 10 cycles, ''phase 1'' is shown by the small circles (maximum downstream forcing), and (b) definition of the four phases considered in this study.

The Digimage tracking operates better if some stationary ''reference lights'' are present in the field of view of the video camera. These reference lights were also used to provide the time reference of the video records: the light emitting diodes used for this purpose were actually lit according to a signal derived from the PC controlling the rotation rate of the table and a Digimage utility was then be used to begin the tracking of the particles at very accurate positions on the video tape. Figure 3 defines the various kinds of temporal averages performed during the processing of the velocity data. ''Instantaneous'' velocity fields are first computed using a time-averaging window of 1 s. (This is done inside the Digimage software.) Then, various phase-averaged velocity fields are constructed using some of the instantaneous velocity fields of cycles 11–20 after the start of the forcing (Fig. 3a). Four phases will be considered here (Fig. 3b): when the offshore flow is maximum in the downstream direction (''phase

[1] The time step of the tracking was fixed to 0.1 s.

[2] Since the aim is to measure residual currents that are of the order of 1 mm s^{-1} (see section 5), one has to wait a long time between separate experiments (several hours) in order to ensure that any spurious current has been dissipated before the forcing begins.

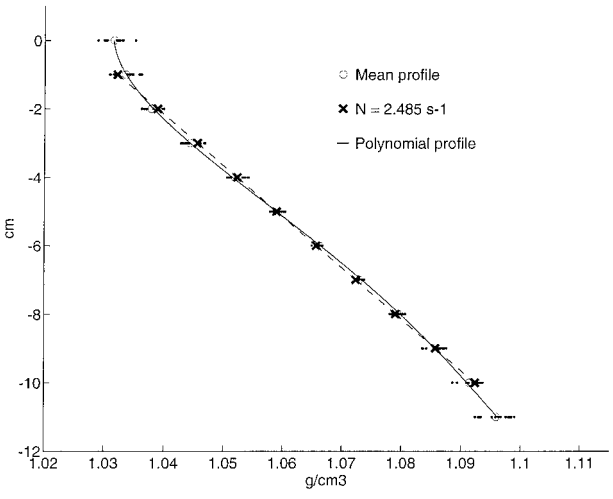

FIG. 4. Density profiles measured prior to the experiments. These profiles result from three stratifications with different mean densities (so that the particles would float close to the various level of interest; see text); the mean density in each profile was set to the value of the mean density of all the profiles, allowing them to collapse on this plot. A linear interpolation of the mean background profile (asterisks) in the range $-11 < z < -1$ cm then gives a typical Brunt–Väisälä frequency that is close to 2.5 s^{-1} (×'s); the analytical profile fitting the average background profile, which was used to initialize the numerical model, is also shown (○'s).

1''), and then each quarter of a forcing cycle thereafter. The experimental residual velocity field is defined here as the time mean of all the instantaneous velocity fields measured between the beginning of the 11th cycle and the end of the 20th cycle.

c. Establishment of the density stratification in solid-body rotation

The now standard ''two bucket'' method (Oster and Vamamoto 1963) was used to establish a linear density stratification using varying concentrations of salt. The table was then accelerated very slowly until the background rotation rate was reached ($f = 0.5$ s^{-1}). Once established, the rotating stratified fluid was used to perform a number of experiments. As mentioned earlier, vertical density profiles were taken before each experiment. Figure 4 shows that the various experiments induced no significant mixing, thereby allowing several experiments with the same stratification. However, one can see in Fig. 4 that the density profiles are not quite linear from top to bottom. This is due to a number of effects, including the following: (i) the two-bucket method does not give a linear profile when the wet area is a function of the vertical coordinate; (ii) the spinup of the table induces some mixing (filling the tank while it is already rotating would be an improvement); (iii) the free surface of the test tank, if considered as an insulated surface, would lead to a condition of no vertical density gradient; and (iv) the slow but persistent evaporation along the free surface leads to convection having the same effect as number iii above. In Fig. 4, it appears that although effect (i) would lead to a stronger stratification in the upper layers, the other effects weaken substantially the stratification stability close to the surface. Thus, although the overall stability is close to that expected ($N = 2.5$ s^{-1}), a polynomial formulation of the mean background density profile (Fig. 4) was computed for use in the numerical model. In light of Fig. 4, however, one must note that there is some variability in the actual density profile measured in the test tank prior to a given experiment; it is acknowledged that this variability contributes to the experimental uncertainty quantified in the repeatability study of section 5c (where it is shown that its level remains acceptable). Furthermore, numerical simulations performed using either the polynomial stratification or a linear one, did not exhibit fundamentally different residual flow fields at the shelf-break level (section 6c).

Another issue concerning the background state of the fluid is the quality of the solid-body rotation that is observed before starting a given experiment. To prevent the immobile air of the laboratory from exerting a stress on the free surface of the rotating fluid, a lid was installed a few centimeters above it. With this setup, it appeared that the most deleterious effect was due to the imperfect alignment of the axis of rotation with the gravity vector. The bottom of our rotating turntable was modified in order to ensure a alignment of less than 10^{-4} rad. Some (weak) periodic motions were nevertheless observed in the fluid even in the absence of forcing; their period is equal to the rotation period of the table and they are quite well detected by the conductivity probes, which indicated that the vertical amplitude of the background isopycnal oscillations is ~0.1–0.3 mm. This did not lead to any significant topographic rectification, however, as demonstrated by velocity measurements performed in the absence of forcing and exhibiting background residual currents of amplitude ~0.2–0.3 mm s^{-1} only.

4. Numerical model

The numerical algorithms utilized in the majority of today's ocean circulation models rely on first- and second-order finite-difference approximations and structured horizontal grids to discretize the governing equations. Their virtues include the simplicity of their numerical foundation and their robustness. Their disadvantages are a limited geometrical flexibility, low convergence rates as resolution is increased, and good but limited scalability on parallel computers. An alternative, which we adopt here, is numerical approximation techniques of high order on unstructured (finite element) grids.

The specific model we employ, the spectral element ocean model (SEOM), is based on the spectral element method (Patera 1984). The spectral element method can be most concisely described as an *h–p*-type Galerkin

finite-element method in which the horizontal domain of interest is first broken up into a (possibly unstructured) grid of quadrilaterals, and (second) within each of which the solution is represented with a high-order polynomial interpolant. It offers several desirable properties for ocean simulations: geometrical flexibility with a spatial discretization based on unstructured grids, high-order convergence rates, and dense computations at the elemental level leading to extremely good scalability characteristics on parallel computers (Curchitser et al. 1998).

The governing equations are a modified form of the hydrostatic primitive equations in z coordinates with a free sea surface. The only modifications are those necessary to introduce the body forces that arise in the rotating laboratory frame (cf. the appendix). Note that, although formulated in geopotential coordinates, the solution procedure is essentially bathymetry following since the three-dimensional elements are isoparametrically mapped to the bathymetry and annular sidewalls as part of the solution procedure. The velocity boundary conditions at the top and bottom surfaces are the kinematic boundary conditions of no-normal flow, and the dynamic boundary conditions specifying the stresses at the sea surface (taken to be zero) and the bottom.

The spatial discretization in SEOM relies on isoparametric and conforming hexahedral elements (cubes with curved surfaces). The three-dimensional variables in each element are approximated with a high-order Lagrangian interpolant whose collocation points are the Gauss–Lobatto roots of the Legendre polynomials (Boyd 1989). The orders of the interpolation in the vertical and horizontal directions are independent, so they can be adjusted individually to achieve the best h–p balance. In the horizontal, the collocation points representing surface pressure (height) are staggered with respect to those of the horizontal velocity in order to eliminate spurious pressure oscillations when the barotropic flow is almost divergence free (Iskandarani et al. 1995). The horizontal elemental partition employed in the simulations below is shown in Fig. 5. A seventh-order interpolant (eight by eight ''points'') is applied within each horizontal element.

Given the complicated bathymetry of ocean basins, and the lack of appropriate three-dimensional grid generation software, the elemental partitioning in the vertical is simplified by restricting it to a structured discretization; that is, the number of vertical elements does not vary horizontally. A three-dimensional spectral element grid can thus be produced by stacking vertically a number of two-dimensional grids. Note that the positioning of the elemental boundaries in the vertical is quite general. For example, a single element can be assigned to follow the sea surface, providing uniform vertical resolution in the surface mixed layer irrespective of local water depth and the fact that the underlying elemental structure is terrain following. In the results described below, a uniformly distributed stack of eight, third-order elements (a total of 25 collocation points in each vertical column) has been used. The total number of grid points on the numerical grid is thus approximately one quarter million.

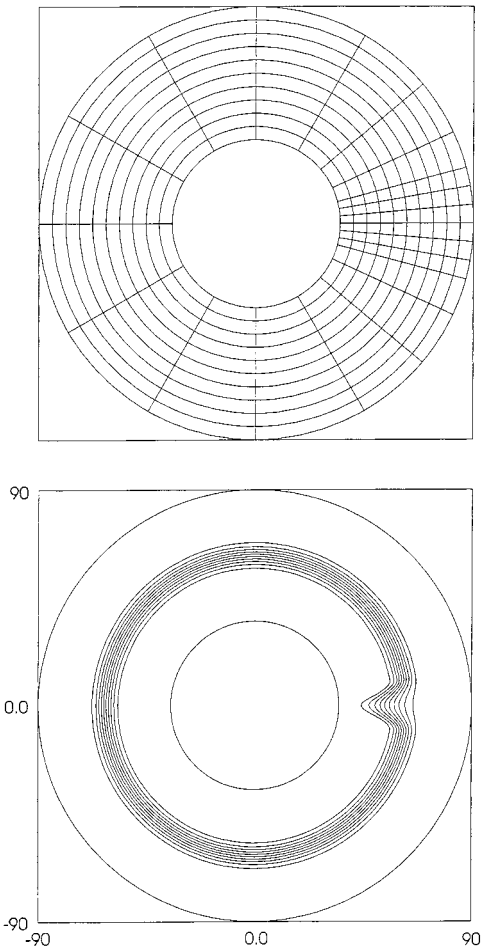

FIG. 5. (top) Elemental partition used in the numerical simulations. A seventh-order interpolant (8×8 points) is applied within each element shown. (bottom) The canyon topography is plotted (the contour levels are in 1-cm increments).

The prognostic variables in SEOM are the horizontal velocity, the temperature and salinity (only one thermodynamic variable, henceforth ''density,'' is needed below), and the surface displacement. The vertical velocity and baroclinic pressure are calculated from the continuity and hydrostatic equations. The temporal discretization is based on a semi-implicit integration scheme. The nonlinear advection term, the Coriolis term, the horizontal viscous term, and the pressure gradient term are integrated with a third-order Adams–Bashforth scheme. The vertical viscous term is integrated with an implicit second-order Crank–Nicholson scheme for enhanced numerical stability. The density equation is also integrated in time with a semi-implicit scheme. The time step used below is 1 ms, a value dictated jointly by the Courant–Freidrichs–Lewy limits

on surface gravity wave propagation and viscous processes.

The parallelization of SEOM relies on a domain decomposition approach in which all vertically aligned elements are assigned to the same processor. Load balancing is therefore assured so long as (approximately) equal numbers of elemental columns are distributed to each processor. Further information on SEOM performance on parallel systems is given in Curchitser et al. (1998). The computations reported below were obtained on the HP Exemplar system at the National Center for Atmospheric Research.

Terrain-following numerical models are subject to a potentially troublesome source of error having to do with the appearance of fictitious unbalanced pressure gradient forces. In the present setting, the easiest way to assess the magnitude of these fictitious forces is to run the numerical model from rest with no forcing. Since the initial isopycnals are level, no circulation should result in this configuration. When we perform this test with SEOM for the central parameters of this article, only trivial [$O(10^{-3})$ cm s^{-1}] currents result, showing the advantages of the high-order method in the limit of steep topography and strong stratification. A complete description of SEOM is given in Haidvogel and Beckmann (1999).

5. Experimental results

As described above, the data obtained in the present experiments were (i) time series measurements of the density field at selected Eulerian locations and (ii) the temporal development of horizontal velocity fields at the observation levels z_1, z_2, and z_3. The former will be considered first.

a. Density time series

Figure 6 depicts the vertical dependence of the amplitude and phase of the density oscillations during forcing cycles 11 and 12, at horizontal location 2 (see Fig. 2). Relation (2) has been used to transform the density data into measures of the time-dependent displacement of isopycnals. The main frequency appears to be that of the forcing (period equal to 24 s). The phase at the shelf-break level ($z = z_2 = -2.5$ cm) is such that the maximum upward elevation is reached slightly before the forcing velocity vanishes (increasing in the downstream direction); recall that the oscillations cycles have a period of 24 s and begin by an increase in the downstream direction (Fig. 3). The isopycnal vertical displacement thus leads the alongshore forcing by roughly 90°; therefore, the vertical velocity is in phase with the alongshore current. (The isopycnals are moving upward when the offshore current is oriented so as to leave the coast on its left, which is indeed the ''upwelling favorable'' direction.) The oscillation at the upper level leads the oscillation at the shelf-break level, and lags

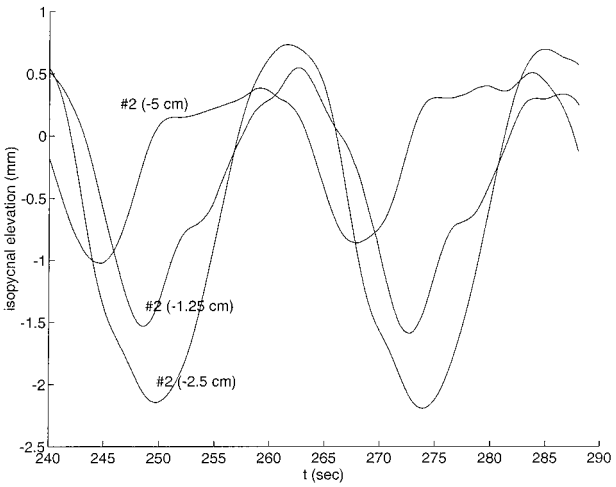

FIG. 6. Vertical dependence of the time series of isopycnal displacements measured at location 2 in the laboratory model. Cycles 11 and 12 are plotted and the period of the forcing is 24 s. At time $t = 240$ s, the velocity far from the canyon is 0 and increasingly downstream.

the oscillation at the lower level. The amplitude is maximum at the shelf-break level, where it reaches ~1 mm; according to the scaling rules mentioned in section 2b(2), it amounts to ~5 m only in oceanic dimensions. The physical model actually exhibited very small vertical isopycnal displacements at all the locations systematically studied in our experiments. These locations are relatively far from the topography (see Fig. 2) and one additional experiment was performed with a probe located at the number-free open-circle symbol in Fig. 2. The amplitude of the oscillations recorded there (along the canyon axis, close to the shelf break) exceeded 6 mm (amounting to 60 m for a crest-to-crest oceanic value). In this experiment the significant vertical excursions thus appear to be confined to the immediate vicinity of the topography.

Such observations, relevant to the temporal evolution at the forcing frequency, proved to be experimentally repeatable (although no quantitative error analysis of the conductivity measurements was conducted). This is not the case of the low-frequency evolution, however. For example, one can see in Fig. 6 that the mean displacement during cycles 11 and 12 is negative at all depths; the details of the low-frequency evolution, of which the mean displacement at cycles 11 and 12 is an indication, were not found to be very reliable (i.e., experimentally repeatable). The mean isopycnal displacement, however, was consistently found to be small (of the order of 1 mm), at all the locations investigated, including the canyon head, and over the full length of the experiments (20 forcing cycles).

The conclusions to be drawn from the density time series data measured in the laboratory are the following. First, no dramatic residual displacements of the isopycnals are observed. Second, the vertical excursion is weak

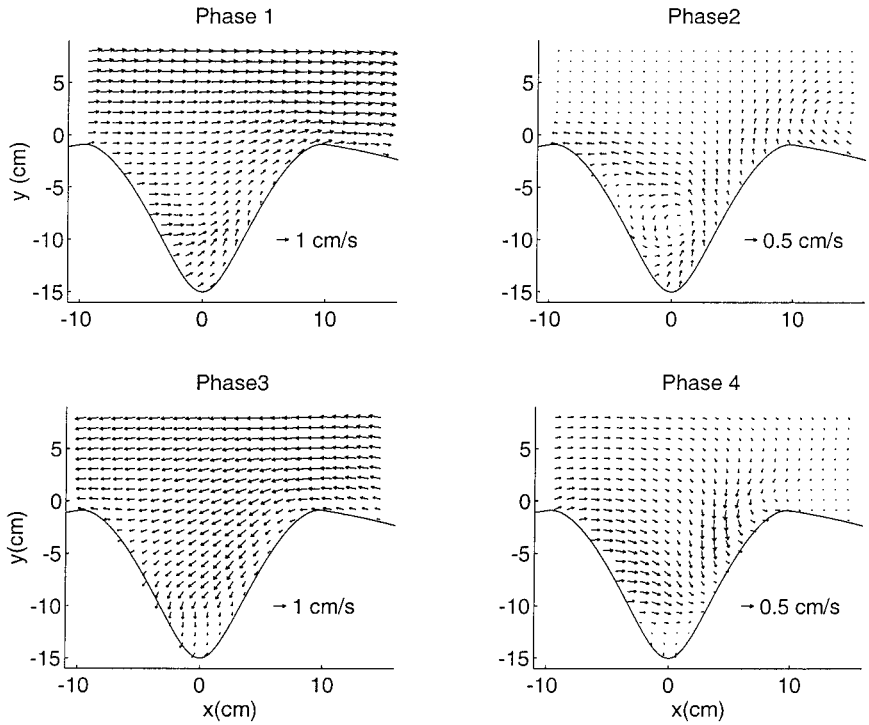

FIG. 7. Laboratory phase-averaged velocity fields obtained at the shelf-break level for the four phases indicated in Fig. 3b. The curved solid lines define the contour of the shelf break.

when translated into oceanic values, except very close to the canyon head.

b. Velocity fields

The velocity fields at levels z_1, z_2, and z_3 in Fig. 2 were investigated in the region extending between (i) $x = -10$ cm and $x = 15$ cm in the alongshelf direction, and (ii) $y = -15$ cm and $y = 8$ cm in the cross-shelf direction. As noted previously, the alongshore direction of increasing x will be referred to as downstream.

1) PHASE-AVERAGED FLOW AND RESIDUAL CURRENTS AT THE SHELF-BREAK LEVEL

Figure 7 shows the instantaneous flow behavior as obtained from the laboratory experiments at the four phases defined in Fig. 3. One notes first an asymmetry in the flow patterns for the maximum rightward (phase 1) and leftward (phase 3) flow phases: while the flow exhibits a tendency to plunge into the canyon and then follow the bathymetry at phase 1, it has the opposite behavior at phase 3; that is, it tends ''first'' (in an advection sense) to follow the canyon bathymetry and ''then'' to cross the rim onto the shelf. Thus the flow appears to be constrained to follow the downstream wall of the canyon but not its upstream wall. One can also note that nonzero flows remain in phases 2 and 4, for which times the background velocity is zero (but decreasing or increasing, respectively). Furthermore these flows are not symmetric: phase 2 is characterized by a cyclonic eddy structure within the canyon whereas phase 4 suggests a broad current from the deep water into the canyon.

As explained earlier, the residual or time-mean current is obtained by averaging the Eulerian flow field over the last 10 oscillation cycles in the 20-cycle dataset. The laboratory structure of the residual flow at the shelf-break level, shown in Fig. 8, is characterized by a weak and wide anticyclonic eddy centered on the upstream ''corner'' of the canyon, and by a small but intense cyclonic eddy near the canyon head, close to the downstream wall. There is a well-defined S-shaped connection between the two residual eddies, indicating that the cyclonic eddy is partly fed by a flux emanating from the anticyclonic one. Another part of the residual flux converging into the cyclonic eddy comes from the shelf upstream of the canyon; note that the maximum residual velocity occurs close to the upstream wall of the canyon. Finally, the spatially fluctuating residual current that issues from the canyon at its downstream corner exhibits a tendency to follow the model continental slope in the downstream direction. The residual current locally exceeds 3 mm s^{-1}, which is a significant fraction of the characteristic forcing amplitude $U = 1$ cm s^{-1}.

Let us consider now the residual vorticity and divergence fields. The former is characterized mainly by a pool of cyclonic vorticity sitting inside the canyon walls,

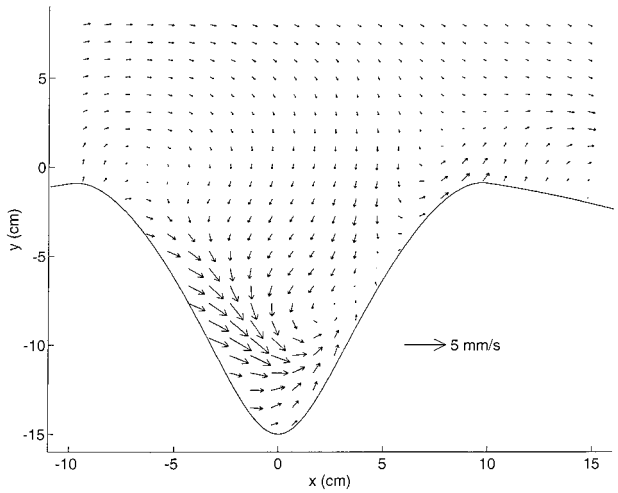

FIG. 8. The mean of the four independent experimental realizations of the residual velocity field at the shelf-break level.

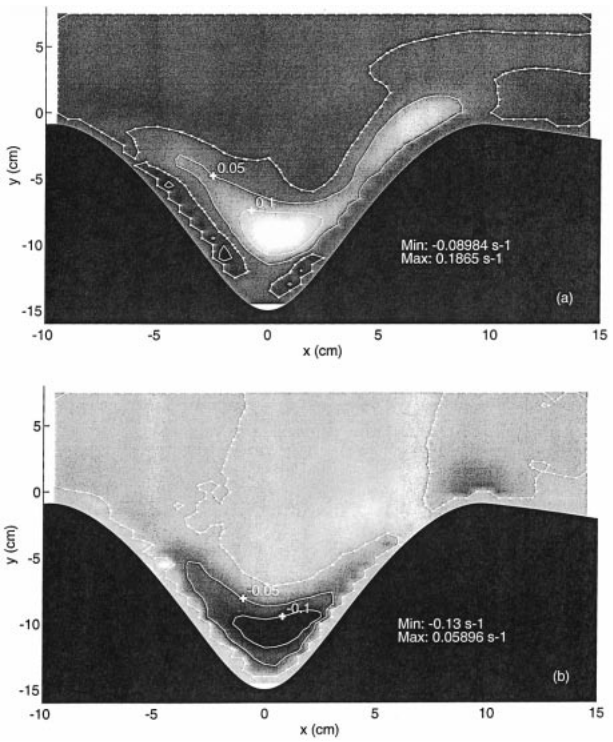

FIG. 9. (a) Residual vorticity and (b) divergence fields at the shelf-break level (laboratory measurements). The contour spacing is 0.05 s^{-1}; the 0 contour is indicated by dots; light (dark) shades correspond to positive (negative) values.

relatively close to the canyon head (Fig. 9a). This residual cyclonic vorticity is not exactly centered on the canyon axis; the pattern is somewhat shifted downstream, with an extension of positive vorticity close to the downstream corner of the canyon. The residual divergence field (Fig. 9b) appears to be more symmetric; the main feature is a convergence zone extending over roughly the same area as the cyclonic pool mentioned above.

2) VERTICAL VARIABILITY

Figure 10 shows the instantaneous flow fields at phases 1 and 3 and levels $z = z_1$ and z_3 (see Fig. 2). At the upper level (upper plots in Fig. 10), one can see that the topography induces little deflection of the flow, especially at phase 1 when the flow is in the downstream direction; this is probably due to the density stratification, which inhibits the upward influence of the bottom topography. Below the canyon rim (lower plots of Fig. 10), the water inside the canyon walls is shielded very efficiently from the laboratory forcing, exhibiting little motion even though the offshore flow is at its maximum.

The residual flow is strongly dependent on the vertical, as one can see in Fig. 11, a plot of the residual currents measured at the upper and lower levels. Above the canyon rim (Fig. 11a), the main feature of interest is a wide and weak residual anticyclonic eddy centered on the upstream corner of the canyon, leading to a basically onshore residual flow along the canyon axis. A pool of stagnant water is also observed on the shelf, downstream of the canyon. Finally, a residual flux separates from the anticyclonic eddy and flows above the model continental slope in the downstream direction. The horizontal residual divergence at this level is less than 0.02 s^{-1} (not shown). At the $z = z_3$ level (Fig. 11b), a ''downstream current'' is the main feature exhibited by the residual flow field at the $z = z_3$ level (Fig. 11b). This current is intensified along the slope, downstream of the canyon, but there is no significant divergence at this level: thus the downstream current is probably fed by horizontal fluxes, which in Fig. 11b appear to come mainly from the sloping region upstream of the canyon, where the residual velocity has an onshore component. (This is more clearly seen in visualizations using an extended display.) Finally, one can note from Figs. 8 and 11 that the residual current is greater for $z = z_2$ than at the $z = z_1$ or z_3 levels. In the vertical direction, the maximum ''rectification'' thus occurs close to the shelf-break level.

c. *Laboratory repeatability*

The experimental uncertainty is due to the imperfect control of the experimental conditions and to the noise introduced by the measurement technique. The repeatability of the velocity measurements was carefully examined by conducting four independent experiments. This analysis was restricted to the shelf-break level owing to the amount of work involved. A ''mean laboratory realization'' was defined by taking, at each point, the average of the measurements obtained in the four (independent) realizations and the uncertainty relative to

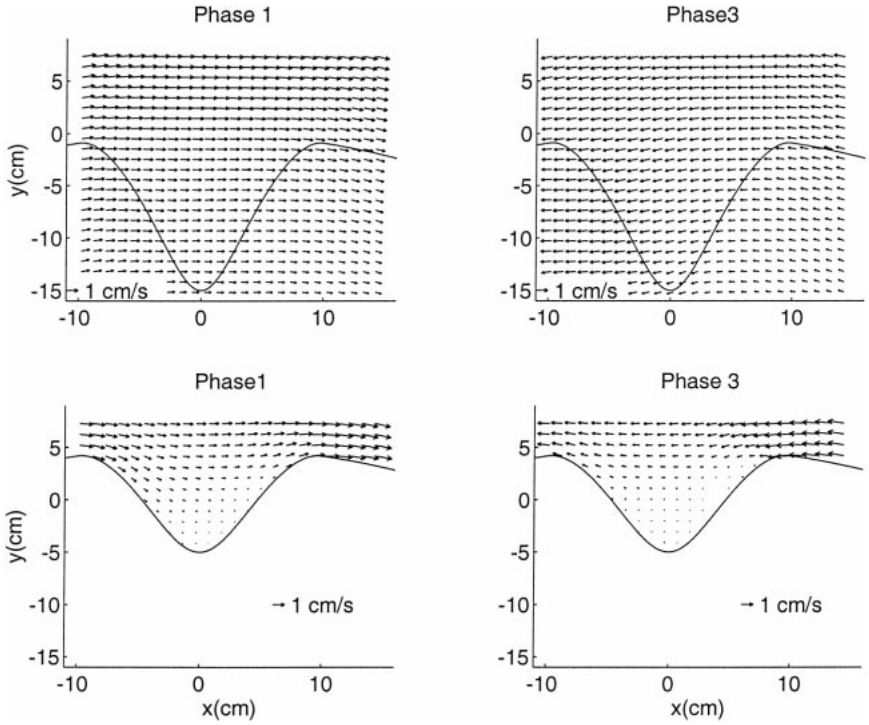

FIG. 10. Laboratory measurements of the phase-averaged velocity fields at the lower and upper levels: upper plots, $z = z_1$ (the curved solid lines are the shelf break); lower plots, $z = z_3$ (the curved solid lines are the $z = -5$ cm isobath).

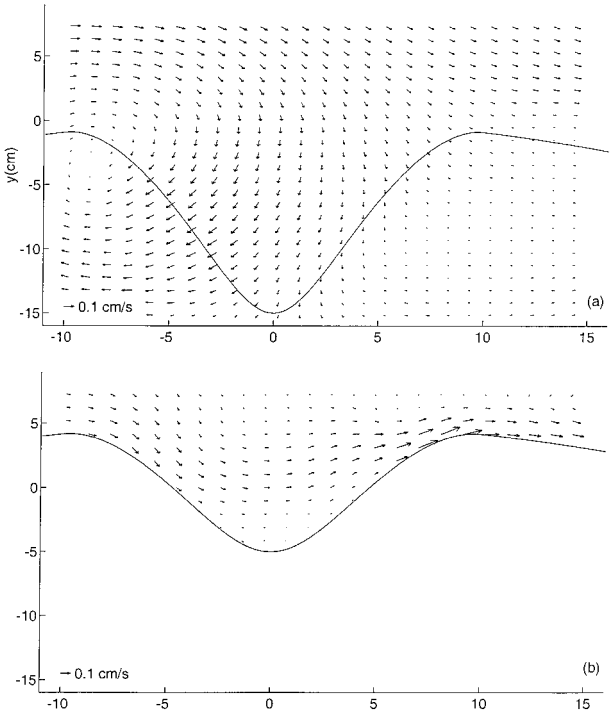

FIG. 11. Experimental residual velocity fields at the (a) upper and (b) lower levels.

this ensemble average was deduced from the departures observed in each particular realization.

This uncertainty will be discussed using spatially averaged (''statistical'') quantities in the display window defined at the beginning of section 5b. The same quantities will also be used when comparing quantitatively the numerical and laboratory results (section 6). It is thus important to know the experimental ''error bars'' that apply to them.

The statistics considered here are spatial averages, at a given level, of (i) the u and (ii) the v components of the (Eulerian) residual velocity in the reference area, and (iii) the spatial average of the residual ''kinetic energy'' $[e_c = (u^2 + v^2)/2]$; these spatially averaged quantities will be noted as $\overline{u}$, $\overline{v}$, and $\overline{e}_c$, respectively. The values thus obtained (at the shelf-break level) for the mean laboratory realization are listed in Table 3, where the spatially averaged residual currents appear to be oriented in the onshore (negative $\overline{v}$) and downstream

TABLE 3. Spatially averaged statistics for the mean laboratory realization, at the shelf-break level.

	$\overline{u}$ (mm s^{-1})	$\overline{v}$ (mm s^{-1})	$\overline{e}_c$ (mm^2 s^{-2})
Phase 1	7.90	0.89	35.88
Phase 2	−0.36	0.88	1.53
Phase 3	−7.31	−2.13	34.30
Phase 4	1.28	−1.20	2.70
Residual	0.37	−0.38	0.46

TABLE 4. Experimental uncertainty of $\bar{u}$, $\bar{v}$, and $\bar{e}_c$ at the shelf-break level.

	$\Delta\bar{u}$ (rms, %)	$\Delta\bar{v}$ (rms, %)	$\Delta\bar{e}_c$ (rms, %)
Phase 1	1	28	<1
Phase 2	18	7	2
Phase 3	1	3	<1
Phase 4	21	8	3
Residual	37	14	5

(positive $\bar{u}$) direction. The statistics obtained for the phase-averaged flow are also mentioned in Table 3, where it appears, for instance, that the amplitude of the spatially averaged alongshore velocity, $\bar{u}$, is larger at phase 1 than at phase 3, suggesting a greater topographic drag when the flow is in the upstream direction. Such a conclusion, however, remains tentative as long as the uncertainty pertaining to the values mentioned in Table 3 has not been specified. This experimental uncertainty was quantified by defining the following nondimensional ratios:

$$\Delta\bar{u} = \frac{\frac{1}{N}\sum_{n=1}^{N}(u_n - u_n^{\text{ref}})}{(\bar{u} + \bar{u}^{\text{ref}})/2},$$

$$\Delta\bar{v} = \frac{\frac{1}{N}\sum_{n=1}^{N}(v_n - v_n^{\text{ref}})}{(\bar{v} + \bar{v}^{\text{ref}})/2}, \quad \text{and}$$

$$\Delta\bar{e}_c = \frac{\frac{1}{N}\sum_{n=1}^{N}[(u_n - u_n^{\text{ref}})^2 + (v_n - v_n^{\text{ref}})^2]/2}{(\bar{e}_c + \bar{e}_c^{\text{ref}})/2}, \quad (3)$$

where N is the number of points in the display window, (u_n, v_n) is the residual velocity at each point, and the overbar designates a spatial average. The superscript "ref" corresponds to the data of reference, in this case the mean laboratory realization.

Thus for each realization, the departure from the mean realization was measured by three error coefficients: $\Delta\bar{u}$, $\Delta\bar{v}$, and $\Delta\bar{e}_c$. The rms values of these coefficients (defined on the ensemble of the four realizations) are listed in Table 4. Concerning the phase-averaged currents, the relative uncertainty becomes smaller as the quantity investigated gets larger: $\Delta\bar{u}$ is only 1% at phases 1 and 3 but rises to 20% at phases 2 and 4, when $\bar{u}$ is reduced $\sim$1 mm s^{-1}. We would expect the same error to apply on the cross-shore velocity $\bar{v}$, which is always $\sim$1 mm s^{-1}, but it actually appears to be more repeatable at most phases. The relative error on the kinetic energy statistic is small at all phases (Table 4). Concerning the residual currents, there is a substantial relative uncertainty for $\bar{u}$ and $\bar{v}$ although the various experimental realizations of the residual flow field compare well, visually, to each other (not shown). This relatively high uncertainty on $\bar{u}$ and $\bar{v}$ is certainly due to the fact that these quantities are dimensionally very small (<0.4 mm s^{-1} see Table 3) and are thus easily contaminated by background currents, even if the latter are small (section 3c). The spatially averaged, residual kinetic energy, however, is a more reproducible quantity: its experimental variance is 5% only.

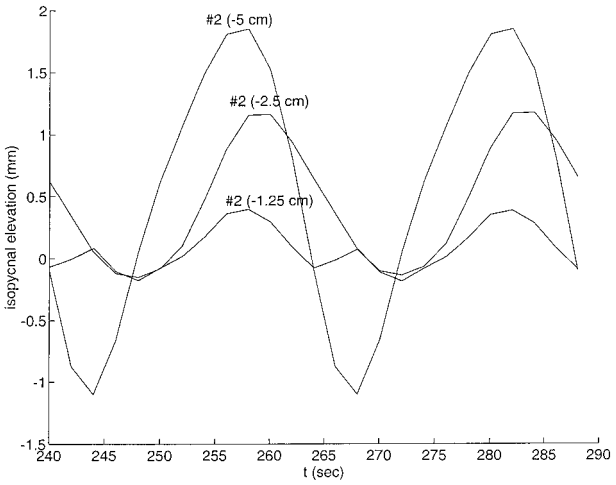

FIG. 12. Numerical results corresponding to Fig. 6. Note that the temporal resolution of this numerical output is much smaller that the one used for the computation itself.

6. Numerical results and comparison to the laboratory measurements

a. Isopycnal displacements

The isopycnal elevation time series from the numerical model, like the laboratory ones, exhibited only small vertical excursions and residual elevations at the locations considered. This is shown, for example, in Fig. 12, which depicts the isopycnal elevations at horizontal location 2, obtained from the numerical model. These numerical results can be compared directly with the laboratory measurements of Fig. 6. The phase relationships between the density fluctuations at the various levels are approximately the same in both models, but the numerical curves lead their laboratory counterparts at all levels. While the amplitudes have a similar magnitude in the laboratory and numerical models, there are differences in the details of the observations: for instance, the maximum amplitude is observed at the shelf-break level in the laboratory but the amplitude increases with depth in the numerics.

b. Velocity fields

1) PHASE-AVERAGED FLOW AND RESIDUAL CURRENTS AT THE SHELF-BREAK LEVEL

Figure 13 is a phase-averaged sequence of horizontal velocity fields obtained at the shelf-break level; these numerical fields are the counterparts of the laboratory velocity fields given previously in Fig. 7. Note that in

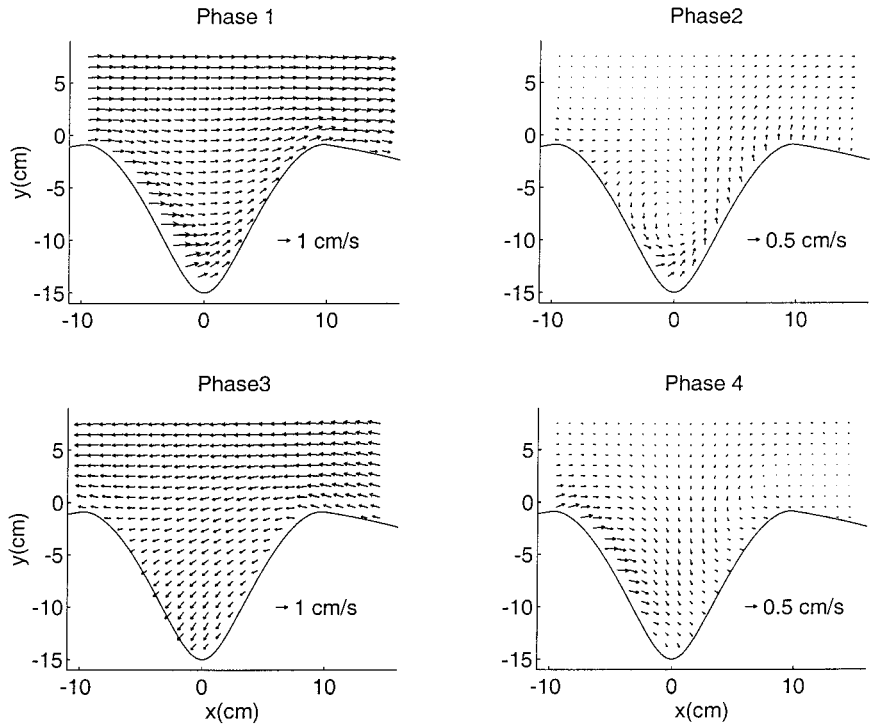

FIG. 13. Numerical results corresponding to Fig. 7.

order to allow for a better visual comparison to Fig. 7, the spatial resolution of the numerical solution was not maintained in Fig. 13 (only one vector every centimeter is plotted, in both directions). There is good qualitative agreement between the numerical results and the laboratory measurements. For example, the asymmetry between phases 1 and 3 is again observed in Fig. 13, where the onshore current along the canyon axis at phase 4 and the cyclonic eddy at phase 2 are also apparent, although the latter is less well defined than its laboratory counterpart.

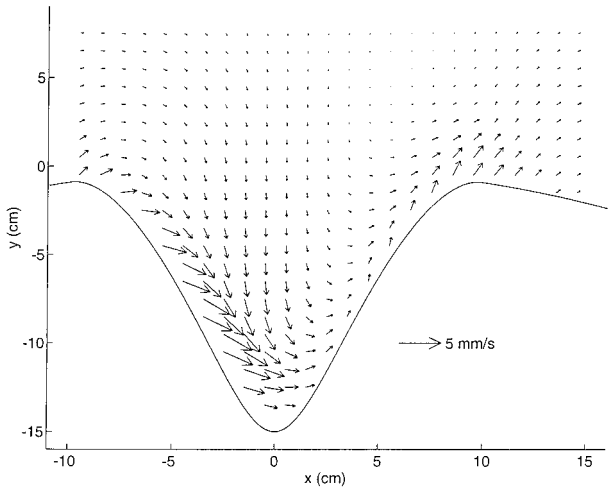

FIG. 14. Numerical results corresponding to Fig. 8.

The residual flow in the numerical experiments was obtained by time averaging the instantaneous results over the duration as the laboratory data. The results for the residual flow of the numerical run depicted in Fig. 13 are given in Fig. 14 (at the shelf-break level). One notes good qualitative agreement with Fig. 8, the corresponding residual flow in the laboratory experiments. The order of magnitude of the residual currents is the same in both models. The anticyclonic loop at the upstream corner is better defined in the laboratory model but still identifiable in the numerical results. The laboratory experiments also exhibit an intensification of the residual current at the upstream wall of the canyon. Finally, as for the numerical experiments, a residual current emanating from the canyon at its downstream corner is also present in the numerical solution.

The differences between laboratory and numerical results are better visualized by subtracting the laboratory residual velocities from the numerical ones. This ''difference field'' is important because it shows that the discrepancies between the laboratory and numerical results are not randomly distributed in space: see Fig. 15. In the canyon area, the numerical model basically appears to generate an ''additional'' residual current flowing along the shelf break and recirculating offshore in a wide cyclonic loop. The statistics of the difference field given in Fig. 15 will be discussed later (section 6c).

The residual vorticity and divergence fields given by the numerical model are drawn in Fig. 16, using the

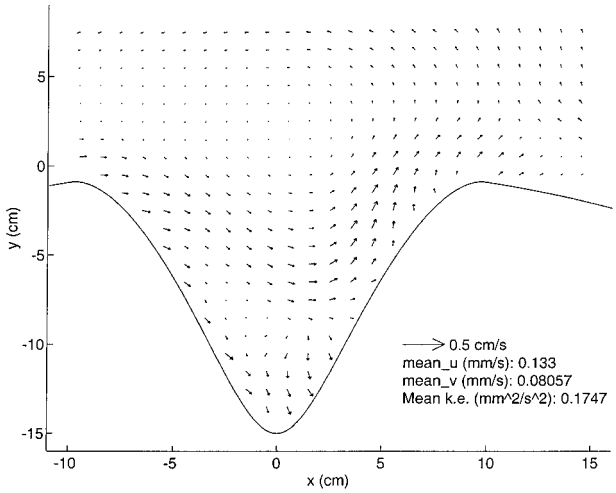

FIG. 15. Vector velocity field representing the difference between the numerical solution and the laboratory measurements.

same procedure as that used for the corresponding laboratory plot of Fig. 9. The quality of the comparison to the laboratory results depends on whether one considers the vorticity or the divergence field. As far as the former is concerned, Fig. 16a exhibits a quite good agreement (with Fig. 9a). Although the maximum vorticity appears to be somewhat weaker in the numerics, the general pattern of the residual vorticity field is visually close to its laboratory counterpart. (See, for instance, the 0.05 s^{-1} vorticity contour.) In contrast, the numerical residual divergence field is strikingly different from that in the laboratory; in Fig. 16b, the convergence area is stretched along the upstream wall whereas in Fig. 9b the convergence occurs in a more compact area close to the canyon head. This could be partly due to the spatial resolution that we could achieve in the laboratory experiments; recall that a spatial averaging was applied in the PTV processing (section 3b), which could be responsible for the smoothing of such a small-scale divergence field as the one seen in Fig. 16b. This possible source of disagreement will be further explored in section 6c.

2) VERTICAL VARIABILITY

Figure 17 shows some phase-averaged velocity fields from the numerical model and can be directly compared to Fig. 10; it shows a visually satisfying agreement between the laboratory and numerical results: small deflection of the flow at the upper level, strong ''shielding'' inside the canyon wall at the lower level. The comparison of the residual velocity fields is more problematic, however.

At the upper level (Fig. 18a), the numerical residual circulation is weaker than its laboratory counterpart (Fig. 11a). The flow consists basically of a current following the isobaths, weakly intensified along the shelf

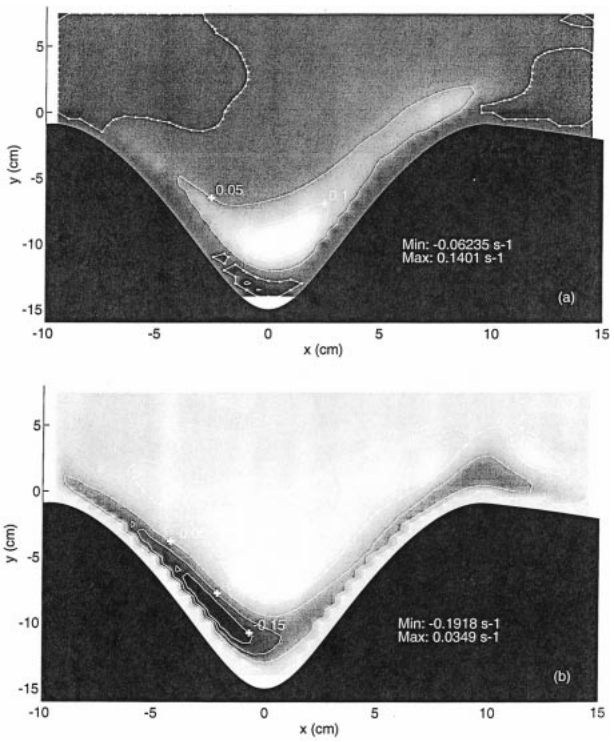

FIG. 16. Numerical results corresponding to Fig. 9. The contour spacing is 0.05 s^{-1}; the 0 contour is indicated by dots; light (dark) shades correspond to positive (negative) values.

break, and partly recirculating into a weak cyclonic eddy located over the downstream corner of the canyon. This residual flow pattern is substantially different from its laboratory counterpart. At the lower level (Fig. 18b), the amplitude of the residual currents generated by the numerical model has the same order of magnitude as that measured in the laboratory, but the rectified current detaches from the sloping region at the downstream corner of the canyon and recirculates into a cyclonic loop, a feature is not observed in the laboratory.

Finally we show a map of the residual vertical velocity given by the numerical model at the shelf-break level (Fig. 19). One can see that the residual convergence zone at the shelf-break level (see Fig. 16b) is associated with downward residual velocities. The maximum downward residual vertical velocity is close to 1 mm s^{-1}. Since no significant long-term vertical displacement of the isopycnal was observed in the numerical model, however, this residual velocity appears to be mainly of an Eulerian character.

c. Quantitative comparison to the laboratory results

The differences between the numerical and laboratory solutions of the canyon flow problem can be further quantified by applying, to the numerical results, the procedure that was used in section 5c to study the experimental uncertainty. This will provide a global esti-

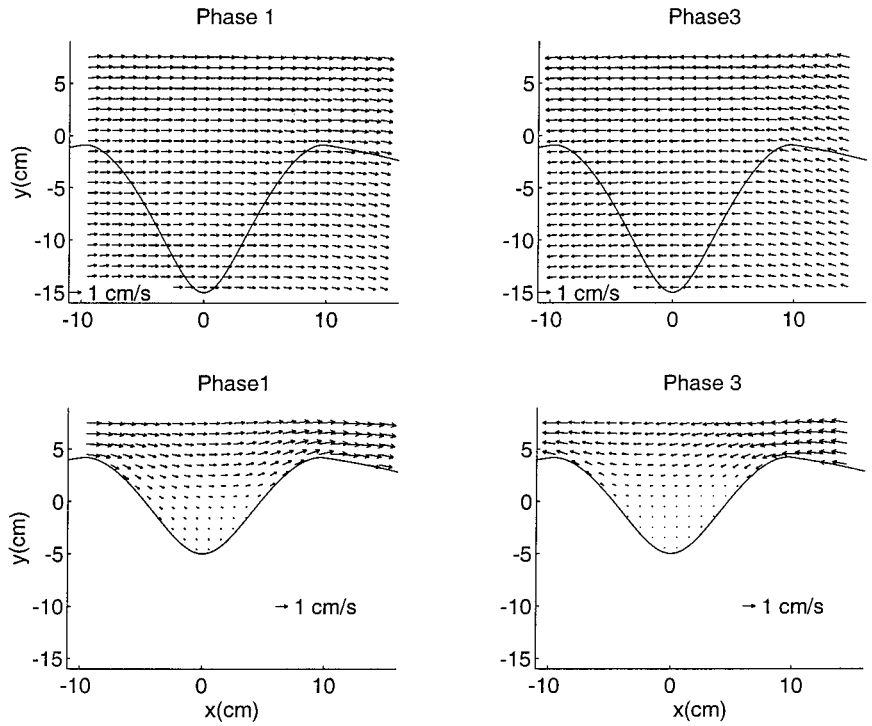

FIG. 17. Numerical results corresponding to Fig. 10.

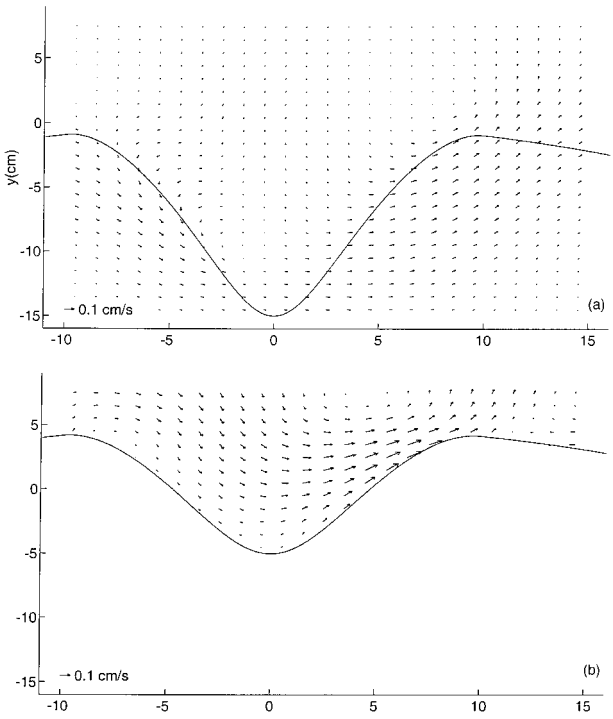

FIG. 18. Numerical results corresponding to Fig. 11.

mation of the departure, from the average laboratory realization (i.e., Table 3), of the numerical results, and allow us to see whether or not this departure lies within the error bar of the laboratory measurements (i.e., Table 4). The numerical values of $\overline{u}$, $\overline{v}$, and $\overline{e}_c$ are thus given in Table 5 for the phase-averaged and residual currents, at the shelf-break level. The difference between numerical and laboratory results is also documented by the values of $\Delta\overline{u}$, $\Delta\overline{v}$ and $\Delta\overline{e}_c$ that one gets when applying the formula of Eq. (3) to the numerical solution (the data of reference then being the mean laboratory realization).

Concerning the spatially averaged alongshore com-

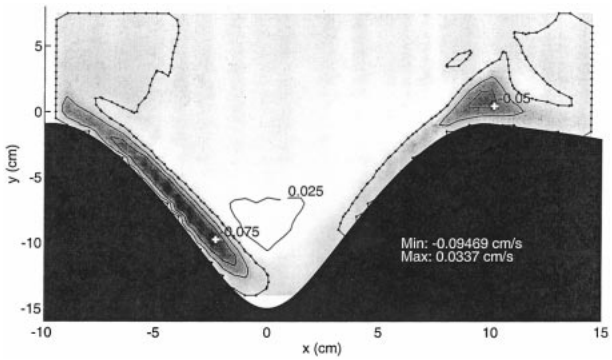

FIG. 19. Time-mean vertical velocity given by the numerical model at the shelf-break level. The contour spacing is 0.025 s^{-1}; the 0 contour is indicated by dots; light (dark) shades correspond to positive (negative) values.

TABLE 5. Spatially averaged statistics from the numerical results (final configuration, shelf-break level) and their relative difference with the laboratory data.

	$\overline{u}$ (mm s^{-1}), $\Delta\overline{u}$ (%)	$\overline{v}$ (mm s^{-1}), $\Delta\overline{v}$ (%)	$\overline{e_c}$ (mm^2 s^{-2}), $\Delta\overline{e_c}$ (%)
Phase 1	8.58, +8	0.38, −80	40.13, 4
Phase 2	0.19, <−100	0.50, −55	0.94, 35
Phase 3	−7.43, +2	−1.31, −48	33.19, 3
Phase 4	0.73, −54	−0.76, −45	1.50, 42
Residual	0.52, +34	−0.30, −25	0.72, 36

ponent of the phase-averaged velocity fields, Table 5 shows quantitative agreement between both models when the currents are strongest ($\Delta\overline{u} \sim 5\%$ at phases 1 and 3) but a relatively strong disagreement at the other phases. At phases 2 and 4, however, $\overline{u}$ is small (<1 mm s^{-1}), and the very large percentage error at phase 2 is due to the fact that the sign of $\overline{u}$ at this particular phase is actually different in the laboratory and numerical models; nevertheless, the two fields compare favorably from a visual point of view (Figs. 7 and 13) and the coefficient $\Delta\overline{e}_c$ remains reasonable (35%). Table 5 also shows that the *amplitude* of the spatially and phase averaged cross-shore current is always smaller in the numerical model (negative $\Delta\overline{v}$ at all phases) although the alongshore forcing is well represented (actually, the numerical $\overline{u}$ exceeds slightly the laboratory value at phases 1 and 3; see Table 5): the currents have a tendency to be less deflected by the topography in the numerical model than in the laboratory experiments. Finally, one can note that the statistic $\overline{e}_c$, which was found to be the less dependent on the laboratory uncertainty (section 5c), is also the most robust when comparing quantitatively the numerical and laboratory data in these experiments. As far as phase-averaged flows are concerned, the relative difference of $\overline{e}_c$ (between both models) ranges from ~4% at phases 1 and 3 to ~40% at phases 2 and 4, the latter value being much larger than the corresponding laboratory uncertainty (Table 4). So there is a significant discrepancy between the laboratory and numerical results at phases where the forcing currents are weak (although both models are in qualitative agreement at all phases): the models are not in perfect agreement concerning the details of the temporal evolution of the flow, as already noticed in section 6a when discussing the density time series.

The statistics for the residual current, also given in Table 5, show that the numerical model generates a greater alongshelf residual current: $\overline{u}$ exceeds the average laboratory value by 34%. (This component leaves the shallow waters on its right in both models.) This difference, however, might not be meaningful owing to the laboratory uncertainty of the $\overline{u}$ measurement (Table 4). Concerning the y component of the residual flow, the spatial average is directed toward the coast in both models, and the same kind of agreement is found, apart from the fact that now the numerical model tends to slightly underestimate its amplitude. The kinetic energy statistic of the residual flow field, however, is significantly greater in the numerical results ($\Delta\overline{e}_c = 36\%$, whereas the laboratory error bar on $\overline{e}_c$ is only ~5%); this owes to the ''additional'' numerical residual circulation already shown in Fig. 15.

This quantitative analysis was restricted to the shelf-break level because the study of the experimental uncertainty was performed at this level only and because, as discussed earlier (section 6b), the laboratory and numerical residual velocity fields are qualitatively different at the other levels (the error statistics are most useful when a qualitative agreement has been observed in the first place).

Before closing this section, we mention here some results obtained in the course of the numerical implementation of the submarine canyon model. Several numerical configurations, numbered 1–5, were actually explored before the ''final'' one was chosen. Runs 1 and 2 used a linear density profile ($N = 2.5$ s^{-1}) whereas runs 3–5 included the polynomial profile mentioned in section 3c. For runs 1 and 3, a free-slip bottom boundary condition was applied and no vertical viscosity was introduced. Run 2 was an attempt to solve the frictional boundary layer (no-slip bottom boundary condition and laminar vertical viscosity). Finally, run 4 made use of the bottom stress law defined in section 2a(2) and run 5 used it together with a laminar vertical viscosity coefficient. The output from run 5 was also processed in order to assess the importance of the spatial filtering introduced by the PTV (as implemented in our experiments). For that purpose, the residual velocity field given by run 5 was filtered using the same averaging procedure utilized in the laboratory processing to generate a regular grid of Eulerian measurements with the randomly spaced Lagrangian estimations (as explained in section 3b). Note that all the plots presented in this article were extracted from the direct results of run 5 (the final configuration), apart from Fig. 15, which derives from the filtered output of the same run.

Table 6 shows that the best agreement, based on the statistics for the residual velocity field, is reached when the bottom stress parameterization is used together with a laminar value of the vertical viscosity (run 5, i.e., the final configuration). It is interesting to note that the residual flow pattern from run 2 was found to be very different from the other ones. A cyclonic eddy then appeared close to the downstream edge of the canyon (not shown). This is most probably due to the fact that the vertical grid spacing used in the numerical computations is not small enough to adequately resolve the frictional boundary layer. Apart from that, the residual currents at the shelf-break level do not appear to be very sensitive to the details of the background stratification (compare runs 1 and 3 in Table 6, for instance). Finally, it was observed that the filtering of the residual velocity field given by run 5 leads mainly to a lesser intensification of the residual current along the upstream edge

TABLE 6. Residual fields obtained at the shelf-break level from various numerical configurations: relative difference with the laboratory data.

Numerical run	Density profile	Bottom condition	Vertical viscosity ($cm^2\ s^{-1}$)	$\Delta\bar{u}$ (%)	$\Delta\bar{v}$ (%)	$\Delta\bar{e}_c$ (%)
1	Linear	Free slip	0	66	−14	63
2	Linear	No slip	0.01	56	−36	79
3	Polynomial	Free slip	0	57	−25	62
4	Polynomial	Stress law	0	46	−12	44
5	Polynomial	Stress law	0.01	34	−25	36
5 (filtered)	Polynomial	Stress law	0.001	31	−24	33

of the canyon (not shown). Such a velocity field is then more comparable with the laboratory one, supporting the idea that the strong residual currents exhibited along the upstream edge by the numerical model are also present in the laboratory experiments, but that they are smoothed out by our acquisition procedure. However, this does not explain all the differences between the laboratory and numerical results, as shown by Table 6 where the nondimensionalised kinetic energy of the difference field still amounts to 33% when the numerical results are filtered (compared to 36% for the nonfiltered data).

7. Concluding remarks

The dynamical setting involves background rotation, density stratification, and steep topography. The study focuses on oscillatory forcing with a single set of parameters ($Ro_t = 0.5$, $Ro = 0.1$, $Bu = 10$). Two different modeling approaches were employed: physical and numerical. The results from both models were plotted so as to allow for a direct comparison of velocity, vorticity, and divergence fields. Residual currents are generated by the nonlinear ''rectification'' of the oscillatory current by the bottom topography. A quantitative (statistical) intermodel comparison of the Eulerian time-mean velocity fields was also performed at the shelf-break level.

In the laboratory experiments, it was observed that for the set of parameters considered here, only small isopycnal displacements were measured (~2 mm). Furthermore the divergence of the residual velocity fields was too small to be reliably measured (with the notable exception of a convergence zone at shelf-break level). The residual circulation thus appears to occur mainly in horizontal planes. This circulation, however, is not the same at each level: below the shelf break, a rectified current fed by an onshore flux exits the canyon and flows along the model continental slope; above the shelf break, a residual anticyclone sitting partly on the shelf, partly on the slope, exchanges water from the sloping region and the model continental shelf. Finally, at the level of the shelf break, there are signatures of both the anticyclone and the alongslope current, and a residual cyclonic eddy is also observed in the canyon area. Furthermore, the measurements clearly show that the residual currents are intensified at this level.

The comparison of the laboratory and numerical results has been surprisingly complex. On one hand the velocities are reproduced accurately at the high flow phases (3%–4% in kinetic energy difference); on the other hand the velocities at near-zero flow phases and the residual currents, while generally satisfactory, are in disagreement by ~30% at the shelf-break level. Nevertheless, even for the residuals, this degree of disagreement, between the laboratory and numerical models, is far better than the discrepancies observed by Haidvogel and Beckman (1999) among various numerical models.

Furthermore, at the shelf-break level, the amplitude and structure of the laboratory and numerical residual vorticity fields are in very good agreement; that is, the numerical results lie within the measurement uncertainty of the laboratory observations. This is not the case for the residual divergence, which is concentrated at the rim of the canyon in the numerical model, but is more widely distributed in the laboratory. An explanation for this difference could lie in the numerical representation of the separation, from the bottom, of the laboratory flow. Figure 13 (numerical model) shows that at phase 1, the horizontal currents are strongly converging while crossing the left-hand canyon rim. By continuity, this convergence indicates a vertical velocity that is likely to be downward owing to the respective directions of the flow and bottom slope. In terms of residuals, this translates into concentrated (negative) divergence and vertical velocities at the left-hand canyon rim (Figs. 16b and 19). On the contrary, in the laboratory the instantaneous (Fig. 7, phase 1) and time-averaged (Fig. 9b) velocity fields exhibit no strong convergence along the left-hand rim, meaning that the flow is mainly horizontal there. Thus the laboratory currents are easily separating from the shelf bottom and flowing over the deeper fluid layers of the canyon, while the numerical velocities exhibit a greater tendency to follow the bottom slope. The vertical separation from the bottom can be initially traced to the dynamics of the frictional boundary layer and is subsequently facilitated by the density stratification. This separation, which is initially controlled by processes occurring at very small vertical scales, is difficult to represent numerically. Such a difficulty is il-

lustrated by the study of the ebbing tidal flow over Knight Inlet by Cummins (1999). Although the field measurements show an early separation of the tidal currents from the oceanic bottom, the separation point is reached a larger distance from the sill in the numerical results. The author concludes that this misrepresentation of the vertical separation is most probably due to the parameterization of the frictional bottom boundary layer (which is not directly solved due to computational constraints) and/or to the fact that the model is hydrostatic. (Consideration of the vertical accelerations might be required for a proper representation of the separation observed in situ.) Given these conclusions, the next natural steps toward a better agreement with the laboratory data would be to increase the vertical resolution and/or to use a nonhydrostatic numerical model.

Greater relative discrepancies appear, however, when the residual circulation at the upper and lower levels is considered; this could be partly due to the fact that the rectification is also less intense at these levels. These differences can be summarized as follows: (i) the rectified current exiting the canyon flows along the sloping region in the laboratory but detaches (horizontally) from the slope in the numerical results (most notably at the lower level), and (ii) no residual anticyclone is observed at the upper level in the numerical results.

It is one of the results of this paper that, thanks to modern acquisition techniques, such differences can be clearly quantified, providing some hints regarding possible areas of improvement for numerical models in this geophysically relevant limit. Different hypotheses are currently being tested in order to operate SEOM in a way that would lead to better agreement with the laboratory results. Given the facts that (i) the laboratory and numerical models were configured with identical forcing and inviscid nondimensional parameters, and (ii) that the numerical model utilized a high-order, contour-fitting numerical algorithm, we conclude that the remaining improvements that could be achieved with the numerical model used here lie in one of two areas: spatial resolution (in particular of the lower boundary layer) and/or congruence between the subgrid-scale assumptions in the numerical model and the actual submillimeter-scale processes in the laboratory.

An important message we take away from this quantitative case study is that it may be quite difficult to achieve (and therefore perhaps we should not expect) ''good'' quantitative agreement between geophysical observations and numerical models, particularly in realistic settings more complex than the one studied here. Implications include the need for systematic means of model–data combination (e.g., via data assimilation) and for careful attention to subgrid-scale parameterization.

Acknowledgments. The feasibility of the laboratory experiments was demonstrated by Xiuzhang Zhang. The operating conditions of the turntable were improved thanks to a design by Leonardo Montenegro. Several students also contributed to this project: Chris Robichaud was instrumental on numerous occasions and actually ran some of the laboratory experiments, which also benefited from the work of Mike Robinson, Kristy Redrick, and William Anderson. Mohamed Iskandarani aided in the analysis of some of the numerical data. The development and present application of the SEOM model were supported by the Office of Naval Research (N00014-93-0197) and the National Science Foundation (NSF, OCE96-19780), respectively. The laboratory experiments were conducted with the support of NSF (OCE96-17639).

APPENDIX

Horizontal Momentum Equations

We write the horizontal[A1] equations of motion in the following way (neglecting viscous effects):

$$\frac{\partial v_r}{\partial t} + (\mathbf{v}\cdot\nabla)v_r - \frac{v_\theta^2}{r} - 2\Omega_0 v_\theta = -\frac{1}{\rho_0}\frac{\partial p'}{\partial r} + F_r + S_r$$

$$\frac{\partial v_\theta}{\partial t} + (\mathbf{v}\cdot\nabla)v_\theta + \frac{v_r v_\theta}{r} + 2\Omega_0 v_r = -\frac{1}{\rho_0 r}\frac{\partial p'}{\partial \theta} + F_\theta + S_\theta,$$

with

$$F_r = 2\Omega_0\omega_1(t)r$$

$$F_\theta = -\frac{d\omega_1}{dt}r$$

$$S_r = 2\omega_1(t)v_\theta + [\omega_1(t)]^2 r$$

$$S_\theta = -2\omega_1(t)v_r,$$

where v_r and v_θ are the radial and azimuthal components of the horizontal velocity; Ω_0 is the rotation rate prior to the (impulsive) change; p' is the pressure perturbation from the pressure p_0, which prevails under centrifugal equilibrium at rotation rate Ω_0; $\omega_1(t)$ is the function of time, which describes the change of rotation rate: $\omega(t) = \Omega_0 + \omega_1(t)$; r is the distance from the center of the turntable; and finally F_r, F_θ, S_r, and S_θ are the forcing terms corresponding to the fact that the rotation rate of the reference frame is changing. The models introduce an oscillatory forcing: $\omega_1 = \Omega_1 \sin(\omega_0 t)$, where $\omega_0 = 2\pi/T$ is the forcing frequency.

REFERENCES

Boyd, J. P., 1989: Chebyshev and Fourier spectral methods. *Lecture Notes in Engineering,* Vol. 49, Springer-Verlag, 798 pp.

Boyer, D. L., X. Zhang, and N. Pérenne, 1999: Laboratory observations of rotating, stratified flow in the vicinity of a submarine canyon. *Dyn. Atmos. Oceans,* **31,** 47–72.

Cummins, P. F., 1999: Stratified flow over topography: Time-depen-

[A1] The model introduces no forcing term in the vertical direction.

dent comparisons between model solutions and observations. *Dyn. Atmos. Oceans,* in press.

Curchitser, E. N., M. Iskandarani, and D. B. Haidvogel, 1998: A spectral element solution of the shallow-water equations on multiprocessor computers. *J. Atmos. Oceanic Technol.,* **15,** 510–521.

Dalziel, S. B., 1992: Decay of rotating turbulence: Some particle tracking experiments. *Appl. Sci. Res.,* **49,** 217–244.

Davies, A. M., 1987: Spectral models in continental shelf sea oceanography. *Three-Dimensional Coastal Ocean Models,* N. Heaps, Ed., Coastal and Estuarine Sciences, Amer. Geophys. Union, 71–106.

Freeland, H., and K. Denman, 1982: A topographically controlled upwelling center off southern Vancouver Island. *J. Mar. Res.,* **40,** 1069–1093.

Haidvogel, D. B., and A. Beckman, 1998: Numerical modeling of the coastal ocean. *The Sea,* K. H. Brink and A. R. Robinson, Eds., Vol. 10, John Wiley and Sons, 457–482.

——, and ——, 1999: *Numerical Ocean Circulation Modeling.* Series on Environmental Science and Management, Vol. 2, Imperial College Press, 318 pp.

Head, M. J., 1983: The use of miniature four-electrode conductivity probes for high resolution measurement of turbulent density or temperature variations in salt-stratified water flows. Ph.D. thesis, University of California, San Diego, 221 pp.

Hickey, B. M., 1995: Coastal submarine canyons. *Proc. Hawaiian Winter Workshop: Topographic Effects in the Ocean,* U.S. Office of Naval Research and Department of Meteorology and School of Ocean and Earth Sciece and Technology, University of Hawaii, 95–110.

——, 1997: The response of a steep-sided, narrow canyon to time-variable wind forcing. *J. Phys. Oceanogr.,* **27,** 697–726.

Hunkins, K., 1988: Mean and tidal currents in Baltimore Canyon. *J. Geophys. Res.,* **93,** 6917–6029.

Iskandarani, M., D. B. Haidvogel, and J. P. Boyd, 1995: A staggered spectral element model with applications to the oceanic shallow water equations. *Int. J. Numer. Methods Fluids,* **20,** 393–314.

Noble, N., and B. Butman, 1989: The structure of subtidal currents within and around Lydonia Canyon: Evidence for enhanced cross-shelf fluctuations over the mouth of the canyon. *J. Geophys. Res.,* **94,** 8091–8110.

Oster, G., and M. Vamamoto, 1963: Density gradient techniques. *Chem. Rev.,* **63,** 257–268.

Patera, A. T., 1984: A spectral element method for fluid dynamics: Laminar flow in a channel expansion. *J. Comput. Phys.,* **54,** 468–488.

Pérenne, N., J. Verron, D. Renouard, D. L. Boyer, and X. Zhang, 1997: Rectified barotropic flow over a submarine canyon. *J. Phys. Oceanogr.,* **27,** 1868–1893.

Reed, H. L., T. S. Haynes, and W. S. Saric, 1998: Computational fluid dynamics validations issues in transition modeling. *AIAA J.,* **36,** 742–751.

She, J., and J. M. Klinck, 2000: Flow near submarine canyons driven by constant upwelling winds. *J. Geophys. Res.,* in press.